

Article

Optimum Processing of Absorbable Carbon Nanofiber Reinforced Mg–Zn Composites Based on Two-Level Factorial Design

Herman Tuminoh^{1,2,3} , Hendra Hermawan^{2,3}  and Muhammad Hanif Ramlee^{1,2,*} 

¹ Medical Devices and Technology Centre (MEDiTEC), Institute of Human Centered Engineering (iHumEn), Universiti Teknologi Malaysia, Johor Bahru 81310, Johor, Malaysia; herman22@graduate.utm.my

² Bioinspired Devices and Tissue Engineering (BIOINSPIRA) Research Group, Faculty of Engineering, School of Biomedical Engineering and Health Sciences, Universiti Teknologi Malaysia, Johor Bahru 81310, Johor, Malaysia; hendra.hermawan@gmn.ulaval.ca

³ Department of Mining, Metallurgical and Materials Engineering, Laval University, Quebec City, QC G1V0A6, Canada

* Correspondence: muhammad.hanif.ramlee@biomedical.utm.my

Abstract: To prevent a premature failure, absorbable magnesium implants must possess an adequate mechanical stability. Among many ways to improve the mechanical properties of magnesium is by particle reinforcement, such as using carbon nanofiber (CNF). This work reports an experimental design for optimum materials and processing of CNF-reinforced Mg–Zn composites based on a two-level factorial design. Four factors were analyzed: percentage of CNF, compaction pressure, sintering temperature, and sintering time, for three recorded responses: elastic modulus, hardness, and weight loss. Based on the two-level factorial design, mechanical properties and degradation resistance of the composites reach its optimum at a composition of 2 wt % CNF, 400 MPa of compaction pressure, and 500 °C of sintering temperature. The analysis of variance reveals a significant effect of all variables ($p < 0.0500$) except for the sintering time ($p > 0.0500$). The elastic modulus and hardness reach their highest values at 4685 MPa and 60 Hv, respectively. The minimum and maximum weight loss after three days of immersion in PBS are recorded at 54% and 100%, respectively. This work concludes the percentage of CNF, compaction pressure, and sintering temperature as the main factors affecting the optimum elastic modulus, hardness, and degradation resistance of CNF-reinforced Mg–Zn composites.

Keywords: biomedical; carbon nanofiber; corrosion; factorial design; magnesium composite; modulus; powder metallurgy



Citation: Tuminoh, H.; Hermawan, H.; Ramlee, M.H. Optimum Processing of Absorbable Carbon Nanofiber Reinforced Mg–Zn Composites Based on Two-Level Factorial Design. *Metals* **2021**, *11*, 278. <https://doi.org/10.3390/met11020278>

Academic Editor: Tullio Monetta
Received: 10 January 2021
Accepted: 2 February 2021
Published: 5 February 2021

Publisher's Note: MDPI stays neutral with regard to jurisdictional claims in published maps and institutional affiliations.



Copyright: © 2021 by the authors. Licensee MDPI, Basel, Switzerland. This article is an open access article distributed under the terms and conditions of the Creative Commons Attribution (CC BY) license (<https://creativecommons.org/licenses/by/4.0/>).

1. Introduction

Magnesium (Mg) alloys are the most studied biodegradable (absorbable) metals for their usage as materials in temporary medical implants like coronary stents and bone fracture fixation screws [1]. Magnesium is an essential element needed for bone function, and its alloys are characterized by its low elastic modulus (40–45 GPa), which is the closest to that of human bone compared to other metallic biomaterials. In a recent development, bone screws and pins made of Mg–Zn–Ca Zn and Mg–RE (RE: rare earths, mainly Gd or Y) alloys have been approving for clinical use in Korea and Germany [2,3]. However, many believe that the mechanical properties and corrosion (degradation) behavior of Mg alloys are not yet ideal and need further improvement. The combination of limited strength and rapid degradation rate may lead to a premature loss of mechanical integrity of an implant before a fractured bone is entirely healed [4–6]. The characteristics of strength and degradation should be in balance to make sure the bone segments could receive adequate stabilisation during healing [7]. One of the promising methods to improve both strength and degradation of Mg alloys is composite reinforcement by carbonaceous particles [8].

Different forms of carbonaceous particles had successfully used for reinforcing different types of metal alloys, including carbon nanofiber (CNF) [9], graphene nanoplate [10], carbon nanotube (CNT) [11], and carbon fiber [12]. CNF reinforcement enhanced the mechanical strength of CNF-A7XXX composites as high as 89.83 GPa while being chemically stable [13,14]. The limited strength and rapid degradation of Mg alloys used in bone implants can be increased and improved through the addition of CNF. The dispersion of CNF and high interface of CNF-matrix assure the strengthening effect and increase degradation resistance of the composite. However, the use of CNF particles for reinforcing absorbable Mg alloys is still limited. Results from the literature showed the highest average yield strength of 74 MPa is recorded for 1.5 wt % in porous Mg, which was enhanced by 54% compared to porous Mg alone. Fibers are regarded as a potent reinforcing category that influences the composites' directional strength and stability [15]. They transfer strength to the matrix, which influence and enhance its properties as desired [16–18]. A CNF–Mg composite can be fabricated through a powder metallurgy process (PM) with attention to at least four parameters, percentage of reinforcement particles, compaction pressure, sintering temperature, and sintering time [19]. According to Orowan strengthening effect, increasing CNF percentage up to 2% in a metal matrix could increase the mechanical aspect of a composite [16]. The usage of 1% CNF as reinforcement improves the ultimate compressive force to 114 MPa, which represents about a 14% increase to that of pure Mg, as well as hardness improvement by 37% [18]. An increase in compaction pressure increases the contact area between powder particles hence decreases porosity that eventually improves the strength and stiffness of the composite [20,21]. Likewise, increasing compaction pressure decreases composite pore size resulting in a more compact or dense material [22]. Finally, both sintering temperature and time will transform the compacted powders into sintered metals and determine the final structure and properties of the composite [23–25].

The combination of the above four parameters can be determined effectively by using the design of experiment (DOE) method that is suitable for characterization, optimization, and modeling process [26]. A two-level factorial DOE allows an analysis of multiple factors simultaneously while maintaining quality data collection, as shown in the work of Gou, et al. [27]. They analyzed the substantial effect of suspension concentration, sonication time, and vacuum pressure on the pore size of single-walled nanotube using a half-normal plot and regression model without the second-order effect. In the present work, we aimed at determining the optimal materials design and process for absorbable CNF-reinforced Mg–Zn composites fabricated via powder metallurgy process using two-level factorial DOE method. The main factors influencing the stability, mechanical properties, and degradation resistance of the composites were identified in view of potential applications of the composites for orthopaedic implants.

2. Materials and Methods

2.1. Design of Experiment

A two-level factorial design was created by using Design-Expert software (Stat-Ease Version 12, Minneapolis, Minnesota, MN, USA). The design suggested a total of 36 specimens as detailed in Tables 1 and 2. Material composition (Factor A) and process parameters (Factor B, C, and D) were determined according to two-level factorial design (2^{k-1} , where k is the number of independent factors). This design represented a series of experiments to fulfil three responses involving the k factor that has two levels: “low” – and “high” +. A center point for each factor was added in the design which allow us to check the goodness-of-fit of the planar two-level factorial design. As shown in Tables 1 and 2, a total of four factors were evaluated: (1) percentage of CNF (0.1–2.0%) [28], (2) compaction pressure (100–400 MPa) [5], (3) sintering temperature (300–500 °C) [29], and (4) sintering time (1–4 h) [5]. The upper and lower limits for each factor were set accordingly based on previous research. Three responses were measured: (1) elastic modulus, (2) hardness, and (3) weight loss, and served as experimental data input for further DOE analysis and empirical model development. The Design-Expert software was also used to perform

statistical analysis, which was then validated by analysis of variance (ANOVA), regression analysis, and lack of fit test; *p*-values of less than 0.0500 were considered as significant.

Table 1. The level of factors for two-level factorial design.

Factors	Lower Limits	Center Points	Upper Level
Percentage of CNF (%)	0.1	1.05	2.0
Compaction pressure (MPa)	100	250	400
Sintering temperature (°C)	300	400	500
Sintering time (h)	1	2.5	4

Table 2. Full factorial design matrix together with the average screening factor output values.

Run	Factors				Responses		
	Percentage of CNF (wt %)	Compaction Pressure (MPa)	Sintering Temperature (°C)	Sintering Time (h)	Elastic Modulus (MPa)	Hardness (Hv)	Weight Loss after 3 Days (%)
1	0.1	400	300	1	3049 ± 157	49.4 ± 4.2	98
2	0.1	100	500	1	2866 ± 200	52.1 ± 5.3	100
3	2	400	500	4	4435 ± 108	60.1 ± 4.9	55.4
4	2	100	500	1	3868 ± 149	55.3 ± 7.4	59.1
5	2	400	300	4	3990 ± 215	56.2 ± 7.5	57.7
6	2	400	500	1	4685 ± 278	57.8 ± 4.7	54.2
7	0.1	100	300	4	3092 ± 192	48.9 ± 6.1	100
8	2	400	500	1	4607 ± 68	54.2 ± 8.8	53.9
9	0.1	100	300	1	2788 ± 178	53.8 ± 6.2	100
10	2	100	500	1	3764 ± 133	54.3 ± 5.9	60.2
11	0.1	400	500	1	3070 ± 183	57.2 ± 4.7	99.2
12	2	100	300	1	3861 ± 141	53 ± 5.3	58.6
13	0.1	100	500	1	3246 ± 134	48.9 ± 3.9	100
14	1.05	250	400	2.5	3392 ± 125	53.2 ± 4.2	80.3
15	0.1	400	300	4	3180 ± 182	51.7 ± 3.2	99.4
16	2	100	300	4	3775 ± 192	52.1 ± 3.8	59.2
17	2	100	500	4	3914 ± 179	58.5 ± 3.2	60.1
18	0.1	100	500	4	3468 ± 100	49.1 ± 9.1	100
19	0.1	100	500	4	3144 ± 196	52.1 ± 6.2	100
20	0.1	100	300	4	3015 ± 213	49.2 ± 7.2	100
21	2	400	300	1	4603 ± 137	59.8 ± 4.5	58.9
22	2	400	500	4	4541 ± 137	58.1 ± 5.1	51.2
23	0.1	400	500	1	3042 ± 157	54.7 ± 5.5	100
24	0.1	400	500	4	3341 ± 158	52.3 ± 2.5	100
25	0.1	400	300	1	3319 ± 278	48.6 ± 6.3	100
26	2	400	300	4	4072 ± 206	57.9 ± 5.3	57.9
27	2	100	500	4	4359 ± 201	56.9 ± 3.2	60
28	2	400	300	1	4251 ± 246	57 ± 1.6	55.8
29	1.05	250	400	2.5	3439 ± 198	50.8 ± 5.6	80.1
30	2	100	300	1	3766 ± 358	55 ± 3.9	63.6
31	2	100	300	4	3644 ± 153	54.3 ± 3.7	63.1
32	1.05	250	400	2.5	3242 ± 235	50.9 ± 6.8	82.4
33	0.1	400	300	4	3516 ± 168	50.1 ± 4.5	100
34	0.1	100	300	1	3237 ± 174	50 ± 7.3	100
35	0.1	400	500	4	3247 ± 215	52.9 ± 4.9	100
36	1.05	250	400	2.5	3405 ± 257	51 ± 6.2	79.6

2.2. Sample Preparation

The 36 specimens were prepared via powder metallurgy process by firstly dissolving 0.1, 1.05, and 2.0 wt % CNF (Product no.1001897011, Sigma Aldrich, St. Louis, MO, USA) in 15 mL of absolute ethanol using ultrasonication for 1 h. In parallel, magnesium (Mg) and zinc (Zn) powders (99.65% purity, particle size < 0.1 mm, 97:3 (Mg:Zn), Bendosen, Selangor, Malaysia) were mixed in absolute ethanol (Fisher Chemical, Product no.: 67-17-5, Loughborough, UK) using an overhead stirrer (Ika Eurostar 40 Digital, Selangor, Malaysia) for 1 h. The CNF solution was then dropped into the Mg–Zn slurry using a 10 mL dropping pipette and further mixed for 30 min to obtain homogeneity [24]. The mixture

subsequently filtered, and vacuum dried at 60 °C for 12 h. The dried mixture was then mechanically milled using a high-energy planetary mill (Pulverisette P-5, Fritsch GmbH, Idar-Oberstein, Germany) with 20 mm diameter stainless steel balls at 250 RPM for 4 h under argon atmosphere [30] to increase the bonding between CNF and Mg–Zn matrix. Prior to this step, 3% of n-heptane was added to the mixture, and the milling was paused for 6 min every 15 min to prevent excessive cold welding [30]. The ball-milled mixture was then compacted (Factor B) using stainless steel mold under 100–400 MPa pressure for 10 min and subsequently sintered at 300–500 °C (Factor C) for 1–4 h (Factor D) in flowing argon atmosphere.

2.3. Materials Characterization and Testing

The microstructure and chemical composition of the resulted CNF-reinforced Mg–Zn composites were evaluated under a Scanning Electron Microscope with Energy Dispersive X-ray (SEM/EDX, Hitachi TM3000, Hitachi High-Tech, Tokyo, Japan) and an X-ray diffraction (XRD, Rigaku, Tokyo, Japan). The specimen surfaces were prepared using an automated disc grinder using various abrasive layer types, from a 600 to 1000-grit SiC paper. Then the specimens were polished using soft velvet cloth suspended alumina [31]. The XRD was performed using Cu-K α radiation at 40 kV/40 mA with a scan range from 20 to 90 degree and a scan rate of 2°/min. Cylindrical specimens were prepared (10 mm diameter, 10 mm height) for compression, hardness, and degradation testing as shown in Figure 1. The compression test was performed by following the ASTM E9-09 standard at room temperature under a constant crosshead speed of 0.5 mm/minute using a universal testing machine (Instron 8874, Illinois Tool Works Inc., Norwood, MA, USA) as shown in Figure 1. Elastic modulus was determined from the resulted compression test curve by taking an average of three slopes at the elastic regions. The hardness test was performed on polished specimens following the ASTM E384 standard using Digital Hardness Vickers machine (Sinowon, DongGuan, China) with a diamond indenter at 100 gf for 15 s, taken on 10 random points on each specimen.

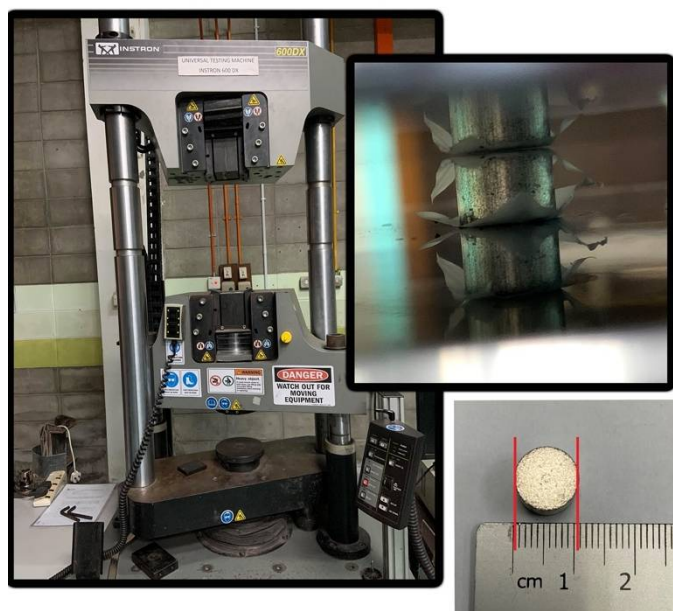


Figure 1. The model of Instron used throughout this study and the specimens were placed on the lower plate of device, which gradually compressed upward. The diameter of each specimen is 10 mm.

The degradation test was performed using a static immersion method in phosphate-buffered saline (PBS, with potassium chloride, Bio Basic Inc, Product no. PD0435, Markham, ON, Canada) at 37 °C without agitation for three days. 10 mL of PBS was used for each specimen having an average weight of 0.85 g. At the end of the test, the specimens were

rinsed using deionised water three times and sonicated for 30 s to remove corrosion products from the surfaces, dried overnight, and weighed using an analytical balance (Uni Bloc, Shimadzu, Kyoto, Japan). The weight loss percentage was calculated from the average weight of three specimens before and after the degradation test.

3. Results

3.1. Elastic Modulus, Hardness and Weight Loss Measurement

From the Table 2, in general, the values are ranging from 2788 ± 178 to 4685 ± 278 MPa where the minimum and maximum elastic modulus demonstrated at run (specimen) 9 and 6, respectively. For hardness, the minimum and maximum are ranging from 48.6 (specimen 25) to 60.1 ± 4.9 Hv (specimen 3). The weight loss reached a minimum for specimen 22 (51.2%) and a maximum (100%) for specimens 2, 7, 9, 13, 18, 19, 23–25, 33–35.

3.2. Microstructural Observation

Figure 2a–c shows SEM micrographs for three groups of specimens that were compacted at a pressure of 400 MPa and sintered at 500 °C for 4 h. The microstructure of Mg–Zn/0.1% CNF indicates the presence of pores (red circle) that are larger compared to those on the other two specimens. The Mg–Zn/2.0% CNF specimens possess a more compact microstructure than those of the others. The EDX analysis detected the presence of elemental magnesium, zinc, and carbon in the overall area of each specimen. The X-rays are emitted in a region of about 2 microns in depth. A randomly taken and multiple line scans for each specimen confirmed a homogenous distribution of the alloying elements. The XRD pattern, Figure 2d, confirms the presence of Mg–Zn peaks in the range of 35–40 degree, indicating the formation of Mg–Zn solid solution, and that carbon particles did not affect the sintering process. The formation of small peak at 38 degree indicating the presence of secondary phase Mg_xZn_y . It was considerably useful for enhancing elastic modulus, hardness and corrosion resistance.

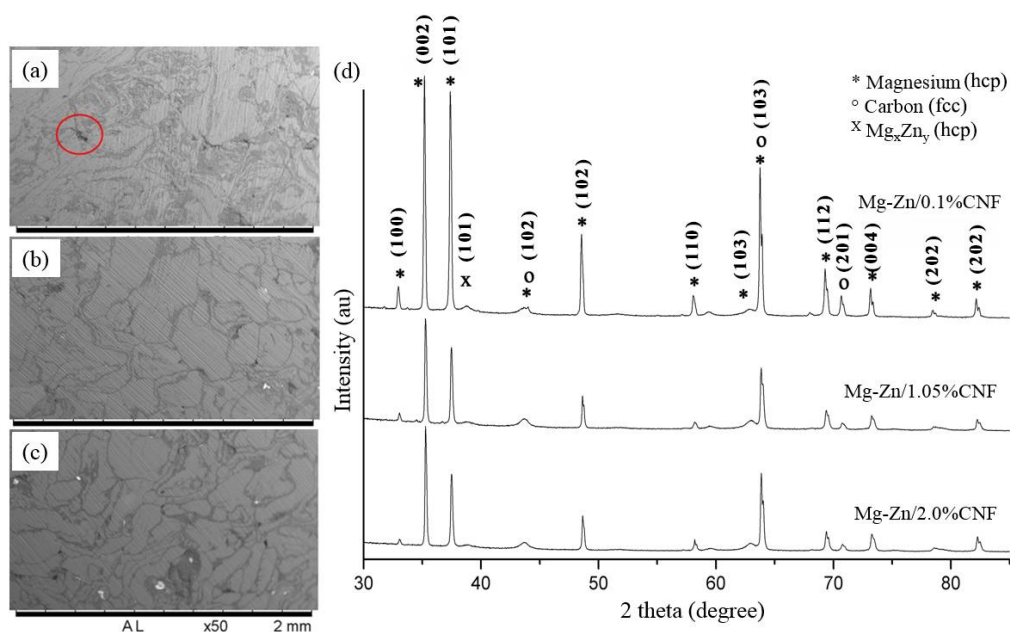


Figure 2. SEM micrographs of: (a) Mg–Zn/0.1% carbon nanofiber (CNF), (b) Mg–Zn/1.05% CNF and (c) Mg–Zn/2.0% CNF, and (d) XRD pattern of the three main phases found in all sintered specimens.

3.3. Half-Normal Plot for Standardized Effect and Analysis of Variance

Figure 3 presents half-normal plots for all responses used for determining the crucial factors influencing the responses by ranking the absolute value of the different effects.

All factors that fall below the regression line (red) are marginal, and the remaining factors and their cross-interaction give considerable impact to the responses, as seen in Table 2. The farther the points are away from the line, the more significant effect is. A screening design of 2^4 was chosen and used to identify the variables that had a higher impact on the responses, which are maximum elasticity and hardness and minimum percentage of weight loss. As recorded in Table 3, the Model F-values for elastic modulus, hardness, and weight loss are 30.44, 9.18, and 1879.06, respectively, implying that the models are significant ($p < 0.0500$).

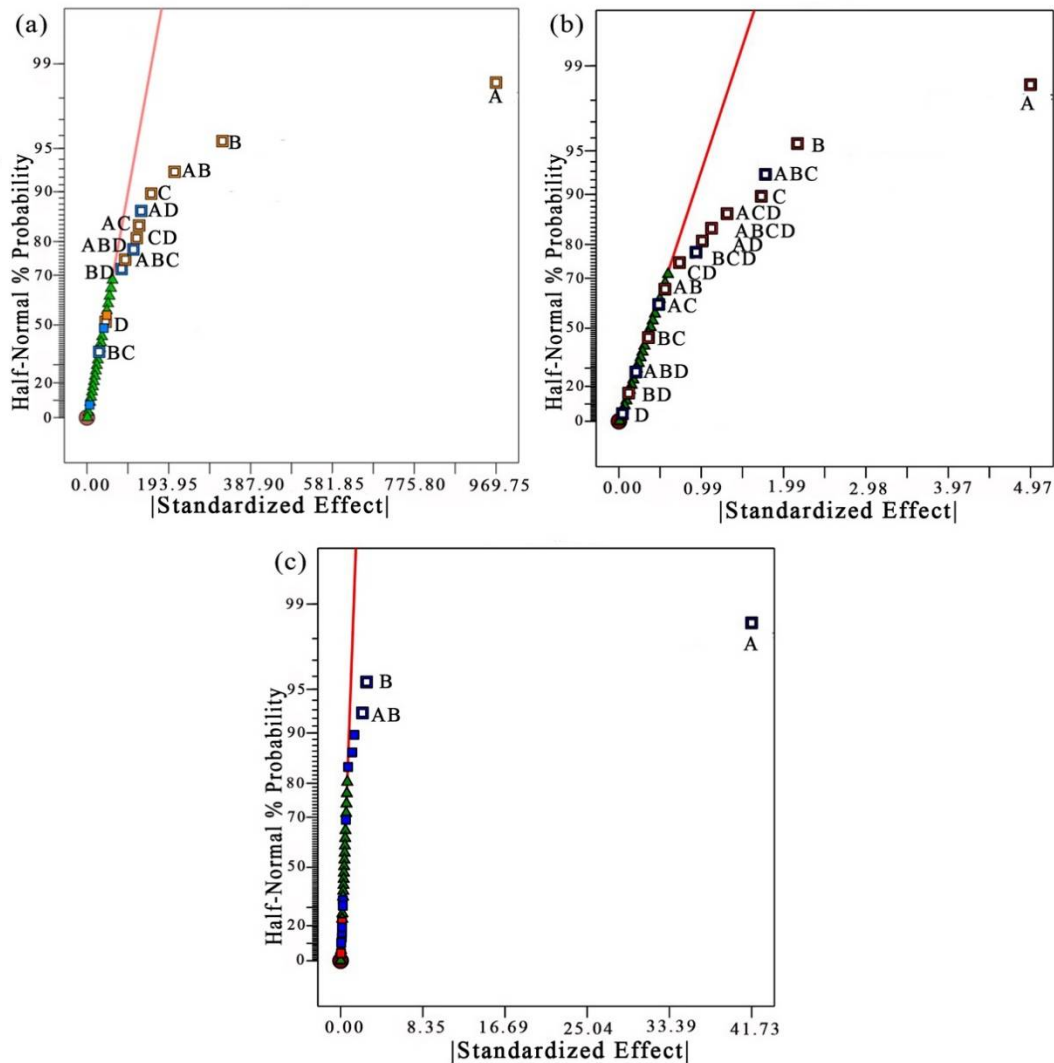


Figure 3. Half-normal plot graph for (a) elastic modulus, (b) hardness, and (c) weight loss.

The $p < 0.0500$ shown in Table 3 indicates the significance of model terms A, B, C, AB, AC, AD, and CD for elastic modulus. Results from the analysis of variance (ANOVA) for hardness show that A, B, C, ABC, and ACD are also significant model terms ($p < 0.0500$). For the percentage of weight loss, as shown in the same table, only A, B, and AB are the significant model terms ($p < 0.0500$), while models C and D are insignificant ($p > 0.0500$). According to statistical data, the model term D (sintering time) is found to be insignificant for all responses ($p > 0.0500$). From the lack of fit (LOF) test, it was found that all responses are insignificant ($p > 0.0500$), implying that the purpose model fits the experimental data, and the independent variables have a considerable effect on the responses.

Table 3. ANOVA for elastic modulus, hardness, and weight loss.

Source	df	Mean Square	F-Value	p-Value	Lack of Fit	
					F-Value	p-Value
Model-Elastic modulus	12	7.907×10^5	30.44	<0.0001		
A-Percentage of CNF	1	7.523×10^6	289.69	<0.0001		
B-Compaction Pressure	1	8.256×10^5	31.79	<0.0001		
C-Sintering Temperature	1	1.861×10^5	7.16	<0.0001		
D-Sintering Time	1	15,753.13	0.6066	0.4444	0.3655	0.787
AB	1	3.457×10^5	13.31	0.0014		
AC	1	1.228×10^5	4.73	0.0407		
AD	1	1.326×10^5	5.11	0.0341		
BC	1	6786.13	0.2613	0.6143		
BD	1	54,120.50	2.08	0.1629		
CD	1	1.119×10^5	4.31	0.0498		
ABC	1	65,884.50	2.54	0.1255		
ABD	1	97,461.13	3.75	0.0657		
Model-Hardness	15	22.14	9.18	<0.0001		
A-Percentage of CNF	1	197.51	81.90	<0.0001		
B-Compaction Pressure	1	37.20	15.42	0.0009		
C-Sintering Temperature	1	23.63	9.80	0.0055		
D-Sintering Time	1	0.0153	0.0063	0.9373		
AB	1	2.48	1.03	0.3237	1.43	0.2435
AC	1	1.85	0.7683	0.3917		
AD	1	8.10	3.36	0.0826		
BC	1	1.02	0.4210	0.5242		
BD	1	0.1128	0.0468	0.8311		
CD	1	4.28	1.77	0.1987		
ABC	1	25.03	10.38	0.0045		
ABD	1	0.3403	0.1411	0.7113		
ACD	1	13.65	5.66	0.0280		
BCD	1	6.94	2.88	0.1062		
ABCD	1	10.01	4.15	0.0558		
Model-Weight loss	3	4675.76	1879.06	<0.0001		
A-Percentage of CNF	1	13,931.98	5598.89	<0.0001	1.36	0.2655
B-Compaction Pressure	1	55.92	22.47	<0.0001		
AB	1	39.38	15.83	0.0004		

3.4. Fit Statistic Calculation

The statistical significance of the models was further checked by other coefficients of regression (Table 4). The R^2 coefficient value of 0.9432 (Response 1) and 0.9945 (Response 3) suggest a good correlation between experimental and predictor variables since 94.32% and 99.45% of the response variation is explainable by the model. The R^2 coefficient value of 0.8788 also indicates a good correlation between the experimental and predictor variables.

Table 4. Regression relation for elastic modulus, hardness, and weight loss.

R^2 /Responses	Response 1	Response 2	Response 3
R^2	0.9432	0.8788	0.9945
Adjusted R^2	0.9122	0.7831	0.9940
Predicted R^2	0.8413	0.5385	0.9927
Adequate Precision	16.2332	9.4642	75.4830

The adjusted R^2 value for Response 1 (0.9122) is close to the predicted R^2 value (0.8413), which indicates that the model has a high accuracy in predicting the response. The predictive models for the screening factors are expressed by Equations (1)–(3), where the variables are coded as +1 (high level) and −1 (low level). The acceptable precision values

were 16.2332 (Response 1), 9.4642 (Response 2), and 75.4830 (Response 3), demonstrating that the model has a strong adequate discrimination ability (the value greater than 4).

$$\text{Elastic modulus} = 3648.56 + 484.88(A) + 160.63(B) + 76.25(C) + 22.19(D) + 103.94(AB) + 61.94(AC) - 64.38(AD) - 14.56(BC) - 41.13(BD) + 59.12(CD) + 45.38(ABC) - 55.19(ABD) \quad (1)$$

$$\text{Hardness} = + 53.80 + 2.48(A) + 1.08(B) + 0.8594(C) - 0.0219(D) + 0.2781(AB) - 0.2406(AC) + 0.5031(AD) + 0.1781(BC) + 0.0594(BD) + 0.3656(CD) - 0.8844(ABC) - 0.1031(ABD) + 0.6531(ACD) - 0.4656(BCD) + 0.5594(ABCD) \quad (2)$$

$$\text{Weight loss} = + 78.92 - 20.87(A) - 1.32(B) - 1.11(AB) \quad (3)$$

Figure 4 illustrates the normal distribution plots of the residual models, showing that the elastic modulus, hardness, and weight loss are normally distributed, as all the points clustered around the diagonal line and are independent of each other. Hence, the normal distribution plots follow the assumption of normality, which specifies that the deviation from the linear is minor. These indicate that all residuals come from a normally distributed population, and the error of variances is homogenous.

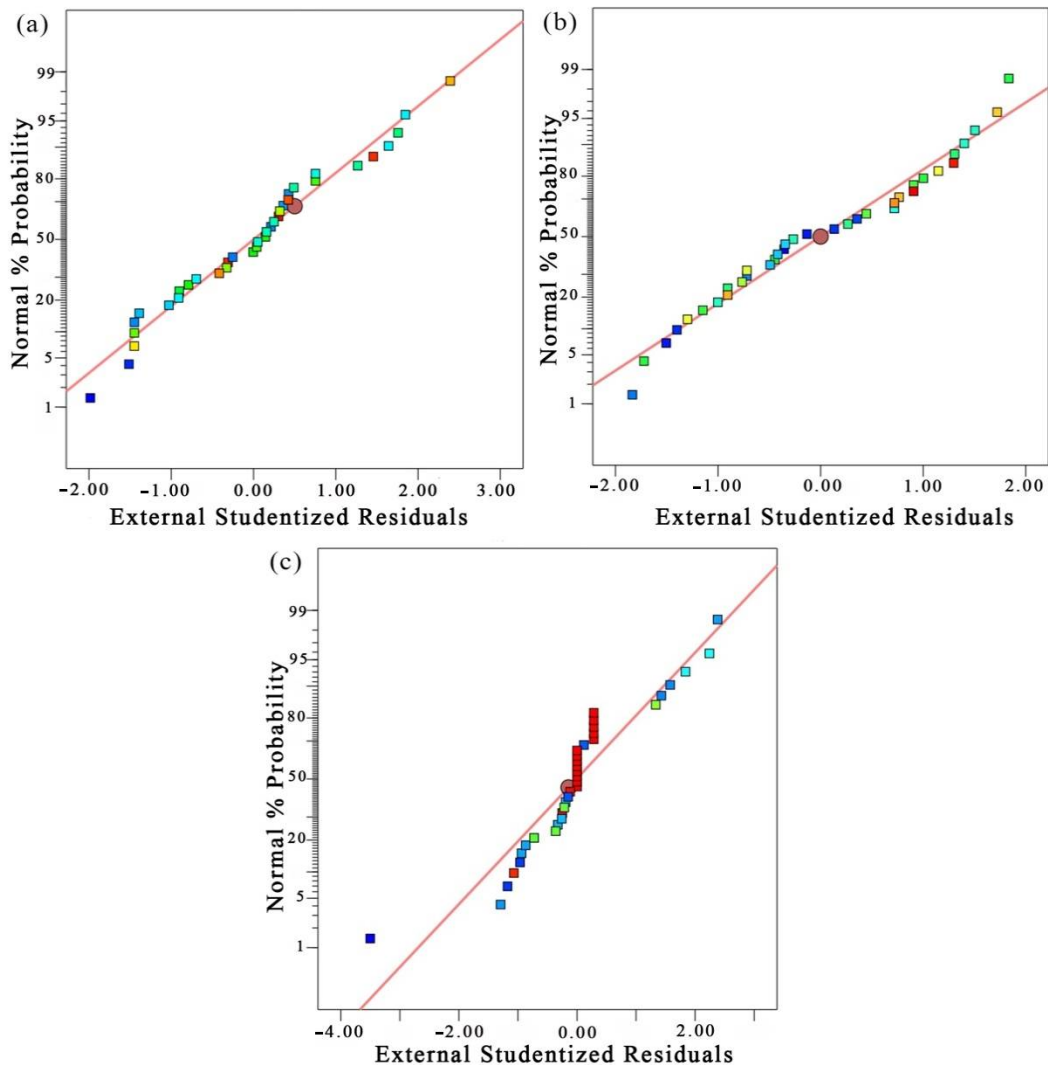


Figure 4. Normal plot of residual for (a) elastic modulus, (b) hardness, and (c) weight loss.

Figure 5 illustrates the perturbation plots, depicting the interaction and effect of corresponding variables towards experimental values. The slope reveals that variables A, B, and C gradually increase the elastic modulus and hardness as their value increase. For the weight loss, it decreases when the variable of A and B increase.

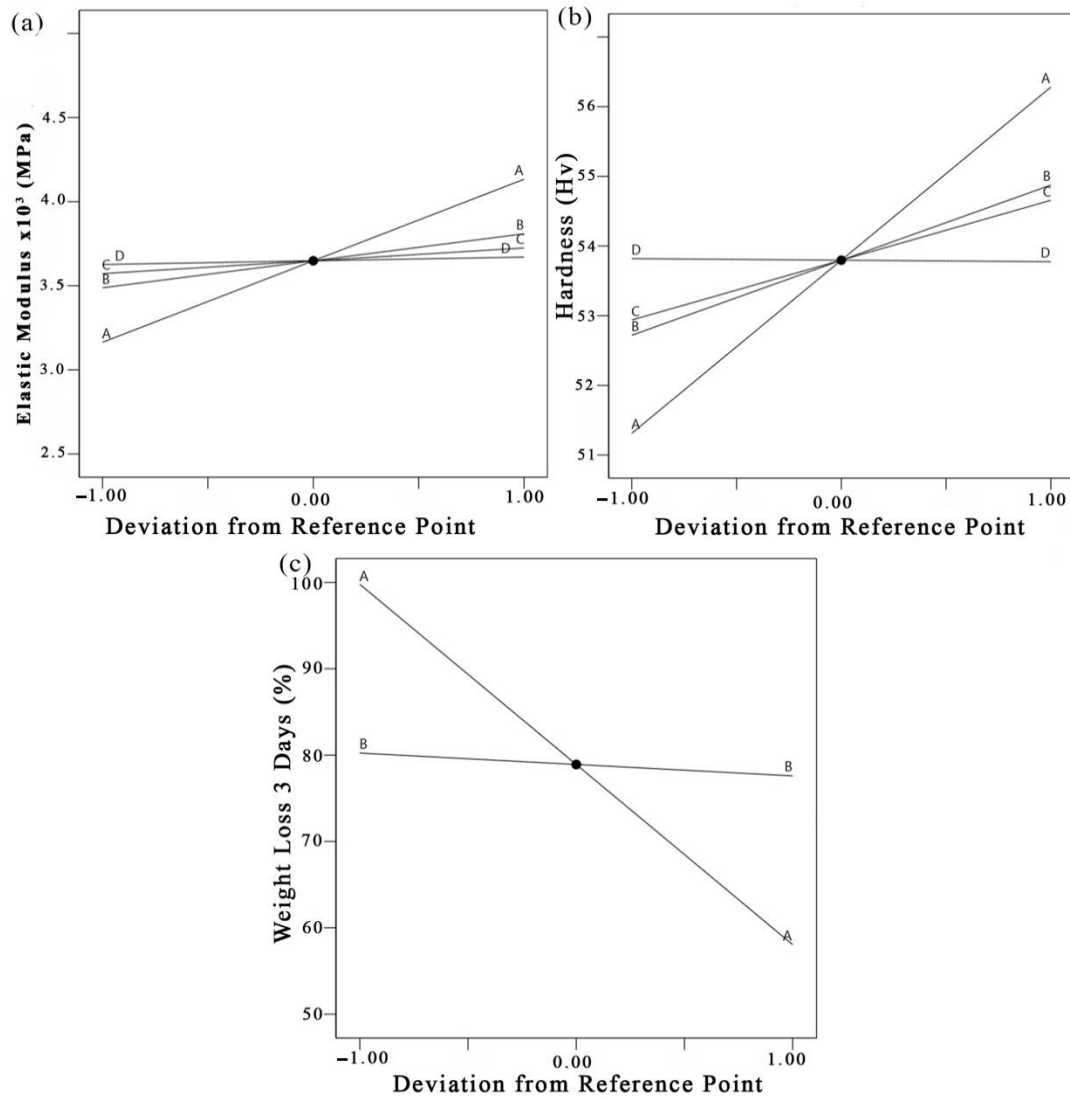


Figure 5. Perturbation plot for (a) elastic modulus, (b) hardness, and (c) weight loss.

4. Discussion

4.1. Analysis of Mechanical Properties

This work was focused on the optimization of composition and fabrication parameters of CNF-reinforced Mg–Zn composites to result in the optimum mechanical properties and corrosion behavior. Based on the graph in Figures 3–5, the percentage of CNF had the most significant effect ($p < 0.0001$) on the mechanical properties (elastic modulus and hardness) of the composites. Based on the perturbation plot in Figure 5, as the content of CNF increases, the elastic modulus and hardness significantly increase as well. The composition of 2.0% CNF resulted in the highest elastic modulus ranging from 3644 to 4685 MPa, with a hardness range of 48.9–60.1 Hv. Besides the particle composition, the strength of the composites is also strongly influenced by the size of the reinforcement particles. The smaller size of the reinforcement particle, like nano-sized CNF, increases the possibility of a strong interface formation between the Mg matrix with the particles [32,33]. A strong

interface assists the load transfer from the matrix to the CNF particles, and vice versa [16,34]. The CNF particles also act as obstacles for the deformation of the matrix when subjected to the load applied during the compression and hardness tests. An effective load transfer capacity and inhibition of dislocation motion by the interfaces reported on a composite of nano-sized carbonaceous particles and AZ91 Mg alloy [35]. A similar mechanism was also observed on a composite of carbon nanotube (CNT) and AZ91D alloy where CNT was responsible for the dislocation strengthening and stress transfer mechanism [36]. Those two mechanisms should also be applicable to the present CNF/Mg–Zn composites and become the reason for the increase of the elastic modulus and hardness by almost 65% and 24%, respectively. Compared to the previous data reported for pure Mg with elastic modulus of 1.86 GPa [37] and 1.6 wt % Mg/CNF matrix with 2687.91 MPa [28], our findings therefore have the highest elastic modulus could have adequate strength and stability to treat fractured bone [37].

Referring to Figure 3 till Figure 5 and Table 2, a significant effect of compaction pressure on the elastic modulus ($p < 0.0002$) and hardness ($p < 0.0009$) is observed on the composites. The optimum compaction pressure of 400 MPa results in a high-density material resulting into the highest elastic modulus (3042–4685 MPa) and hardness (48.6–60.1 Hv). Zou and Lin reported that a maximum hardness was obtained for Mg reinforced with recycled polystyrene after subjected to a compaction pressure of 100 MPa [38]. While Yusof and Zuhailawati found that a compaction pressure of 400 MPa gave the optimum densification of binary and ternary Mg alloys resulting in high hardness (72.9 Hv) and compressive strength (255 MPa) [39]. The present results also reveal the significant effect of sintering temperature ($p < 0.0500$) on the properties of the composites. The highest elastic modulus and hardness were obtained after sintering at 500 °C, an increase of 26% and 24%, respectively, to that obtained at 300 °C. Rai et al. found the maximum hardness and compressive strength of Zn_2Mg_6SiC composite for the sintering temperature of 450 °C compared to 430 °C [40]. Kumar et al. revealed the ultimate compressive strength of 160 MPa for matching maximum compaction pressure (500 MPa) and maximum temperature (640 °C) [41]. This was attributed to the change in the sintering process due to the tight packaging of irregular particles with one another and the removal of obstacles from the sintering route by destroying oxide films from the surface of the particles. Tuminoh et al. [29] found the maximum elastic modulus of 2729.886 MPa when Mg composite was sintered at 250 °C for 4 h which is lower compared to this study. Our result seems to be in agreement with what was reported by Wahi et al. that sintering process at high temperatures resulted in higher densification and mechanical strength [42], and Dlouhy et al. [43], who also reported enhancement of mechanical properties of an alloy matrix sintered at high temperatures. This is because high temperatures increase the kinetic diffusion in sintering process [20].

Sintering under argon atmosphere binds compacted particles using thermal force below the melting point with reducing pressure inside the pores leading to the pore-filling mechanism and production of high-density materials [44,45], besides argon also prevents Mg combustion [24]. At 500 °C, all Zn powders (3 wt % and a melting point of 419 °C) melted and wet the surface of Mg, and CNF particles, promoting a liquid phase sintering mechanism where diffusion may happen between Mg, Zn, and CNF. Luo et al. obtained the highest hardness of 74.3 Hv for Mg–3Zn alloy after being sintered at 560 °C [46]. Similarly, Burke et al. measured the maximum hardness of 65 Hv for Mg after sintering at 500 °C due to the increasing kinetic diffusion between Mg particles [20].

4.2. Analysis of Corrosion Behavior

The results of the static immersion test reveal the significant influence of CNF content on the improvement of degradation resistance of the composites ($p < 0.0001$), with the 2% CNF content resulted in the lowest percentage of weight loss. The presence of CNF particles could help in slowing down the dissolution of the Mg matrix in PBS by increasing the interfacial bonding with the Mg matrix as they are chemically stable in any solution except a powerful oxidizing agent [14]. Similarly, the interfacial effect was observed on a

composite of TiB₂ and aluminium alloy-7010 where the corrosion resistance of composite was 10% higher than the alloy alone [47]. The effect of a strong interfacial bond between aluminium matrix and multi-wall CNF particle in reducing corrosion rate was also reported by Samuel Ratna Kumar et al. as the result of minimal active surface area due to an increase in the percentage of CNF [48]. Referring to Table 2, low compaction pressure resulted in a higher weight loss of the composite, which could be the consequence of a more porous structure that allows PBS to penetrate inside. Increasing compaction pressure contributed to a significant densification and hence an improvement in corrosion resistance as observed for Mg–Zr–Sr–Dy alloys [49]. Increasing compaction pressure up to 500 MPa was found to optimize the corrosion rate of Mg₃Zn₁Ca₁₅Nb alloy to 1.209 mm/year [41]. Similarly, Tahmasebifar et al. observed in their work that corrosion of Mg alloy discs decreased as the compaction pressure increased, from 100 to 250 MPa [50]. According to Mohammed et al. [22], under low compaction pressure, loose powder is formed into porous compacted material and visible microstructure changes as transparent porosity decreases. A small pore formed will assist material to increase the corrosion rate. Nui et al. [51] also observed a corrosion potential of -1.57 V and the lowest corrosion current density of $33.12 \mu\text{A}/\text{cm}^2$ on AZ31 composite sintered at 300 °C.

In biomedical implant application, the major drawback of magnesium alloys is their high corrosion rate in the physiological environment [37]. A high corrosion rates accelerated the degradation of mechanical materials, leading to premature implant failure before tissue-healing is completed. In this study, high percentage of CNF, compaction pressure and sintering temperature significantly increased the elastic modulus, hardness and corrosion resistance of composite. These are particularly relevant for biodegradable orthopaedic implants. In addition, stress when corrosion-assisted will lead to an unexpected premature failure and cracking [52]. It is significant to mention that in PBS solution, magnesium composite was known to be susceptible to stress corrosion cracking [52]. The stress-cracking behaviour of magnesium composite in physiological environments has yet to be investigated before successful application as orthopaedic implants could be tried.

According to ASTM G31-12a, the duration of static immersion test should be determined by the nature and purpose of the test. If the materials that experience severe corrosion, generally, it does not necessarily to lengthy test in obtaining accurate corrosion behavior. The general nature of magnesium's degradation is rapid and thus it is reasonable to predict its corrosion behavior in 3 days [53]. Since that only in vitro study was conducted in the present study, our main focus in degradation test is to evaluate effect of each factors on the degradation of Mg matrix. It is worth noting that the in vitro assessment is usually conducted in a short period particularly for Mg-based material degradation. Longer assessment period is usually performed in animal study (in vivo). In future, an in vivo study which take a longer time (months) to thoroughly evaluate the degradation behavior of this material in a closer-to-human environment will be conducted. In addition, the optimum parameters achieved will be further investigated using response surface methodology (RSM) which can give an ideal and optimum point of each parameter. The assumption of higher limit values could give a better result will be tested and each parameter will be evaluated in a smaller range and response surface contour plot will be developed. 2-level factorial design is a crucial step before RSM by identifying the optimum range and the important parameters. The effect of particle size, toughness and torsional strength will be further evaluated.

There is an increasing demand on innovative clinical orthopedic implants using Mg-based material due to widely recognized as a potentially revolutionary orthopedic biomaterial. The presented results in this paper are valuable for researcher, scientist and engineer to produce biodegradable implant in the future. As suggested by many other researchers from their published papers, the results of elastic modulus, hardness and weight loss is one of the parameters to be considered to develop biodegradable implant [4–6]. In the material design aspect, high mechanical behaviour and corrosion resistant are vital in the application of implant. For example, the higher mechanical strength and corrosion

resistant could facilitate the hard-tissue screw /pin insertion and support long term healing adaptation. Overall, the present work also identifies variables that are non-contributing and insignificant towards the responses. Sintering time has a p -value greater than 0.0500 in all cases, and the duration of sintering time of 1–4 h are unable to improve or decrease the overall response. There seems to contradict the finding of other reported works [23,24], but also in accordance with the writing of Ramli et al. [54] that also found no significant effect of sintering time on the physical and mechanical properties of their composites.

5. Conclusions

A series of carbon nanofiber (CNF)-reinforced Mg–Zn composites were fabricated via powder metallurgy with optimized process parameters based on a two-level factorial design. The effect of CNF composition, compaction pressure, sintering temperature, and sintering time, as the design factors, were statistically analyzed toward elastic modulus, hardness, and degradation rate, as the design responses. The analysis of variance reveals a significant effect for all variables ($p < 0.0500$) except for the sintering time ($p > 0.0500$). The analysis of factorial design reveals that the optimum parameters for fabricating CNF-reinforced Mg–Zn composites resulting into high elastic modulus, hardness, and degradation resistance are 2 wt % of CNF composition, 400 MPa of compaction pressure, and 500 °C of sintering temperature. The elastic modulus and hardness reach their highest values at 4685 ± 278 MPa and 60.1 ± 4.9 Hv, respectively. The minimum and maximum weight loss after three days of immersion in PBS are recorded at 53.9% and 100%, respectively. Finally, this work provides an evidence of the power of factorial design in optimizing experimental parameters for the development of new absorbable materials for biomedical applications.

Author Contributions: Conceptualization, H.T. and M.H.R.; methodology, H.T. and M.H.R.; validation, H.T., H.H. and M.H.R.; formal analysis, H.T., H.H. and M.H.R.; writing—original draft preparation, H.T.; writing—review and editing, H.T., H.H. and M.H.R.; supervision, H.H. and M.H.R.; funding acquisition, M.H.R. All authors have read and agreed to the published version of the manuscript.

Funding: This research was funded by the Ministry of Higher Education Malaysia Fundamental Research Grant Scheme (Grant no.: FRGS/1/2019/TK05/UTM/02/3 and 5F135), Universiti Teknologi Malaysia Tier 2 (Grant no.: 15J84) and Matching Grant (Grant no.: 02M69), and Universiti Kuala Lumpur Collaborative Research Grant Scheme (Grant no.: 4B618).

Institutional Review Board Statement: Not applicable.

Informed Consent Statement: Not applicable.

Data Availability Statement: Not applicable.

Acknowledgments: The authors would like to thank the Canadian Government for providing the Canada-ASEAN SEED scholarship allowing a 6-month research exchange at Laval University (H.T.), Sultan Ibrahim Johor Foundation for scholarship funding (H.T.) and Universiti Teknologi Malaysia for awarding the Research fellowship scheme (H.H.).

Conflicts of Interest: The authors declare no conflict of interest.

References

1. Hermawan, H. Updates on the Research and Development of Absorbable Metals for Biomedical Applications. *Prog. Biomater.* **2018**, *7*, 93–110. [[CrossRef](#)] [[PubMed](#)]
2. Lee, J.-W.; Han, H.-S.; Han, K.-J.; Park, J.; Jeon, H.; Ok, M.R.; Seok, H.K.; Ahn, J.P.; Lee, K.E.; Lee, D.H.; et al. Long-Term Clinical Study and Multiscale Analysis of In Vivo Biodegradation Mechanism of MG Alloy. *Proc. Natl. Acad. Sci. USA* **2016**, *113*, 716–721. [[CrossRef](#)] [[PubMed](#)]
3. Biber, R.; Pauser, J.; Brem, M.; Bail, H.J. Bioabsorbable Metal Screws in Traumatology: A Promising Innovation. *Trauma Case Rep.* **2017**, *8*, 11–15. [[CrossRef](#)] [[PubMed](#)]
4. Krämer, M.; Schilling, M.; Eifler, R.; Hering, B.; Reifenrath, J.; Besdo, S.; Windhagen, H.; Willbold, E.; Weizbauer, A. Corrosion Behavior, Biocompatibility and Biomechanical Stability of a Prototype Magnesium-Based Biodegradable Intramedullary Nailing System. *Mater. Sci. Eng. C* **2016**, *59*, 129–135. [[CrossRef](#)] [[PubMed](#)]

5. Salleh, E.M.; Hussain, Z.; Ramakrishnan, S. Synthesis of Biodegradable Mg-Zn Alloy by Mechanical Alloying: Statistical Prediction of Elastic Modulus and Mass Loss Using Fractional Factorial Design. *Trans. Nonferrous Met. Soc. Chin.* **2018**, *28*, 687–699. [[CrossRef](#)]
6. Bommala, V.K.; Krishna, M.G.; Rao, C.T. Magnesium Matrix Composites for Biomedical Applications: A Review. *J. Magnes. Alloy* **2019**, *7*, 72–79. [[CrossRef](#)]
7. Malizos, K.N.; Papatheodorou, L.K. The Healing Potential of the Periosteum. *Injury* **2005**, *36*, S13–S19. [[CrossRef](#)]
8. Yang, Y.; He, C.; Dianyu, E.; Yang, W.; Qi, F.; Xie, D.; Shen, L.; Peng, S.; Shuai, C. Mg Bone Implant: Features, Developments and Perspectives. *Mater. Des.* **2020**, *185*, 108259. [[CrossRef](#)]
9. Silvain, J.F.; Vincent, C.; Heintz, J.M.; Chandra, N. Novel Processing and Characterization of Cu/CNF Nanocomposite for High Thermal Conductivity Applications. *Compos. Sci. Technol.* **2009**, *69*, 2474–2484. [[CrossRef](#)]
10. Turan, M.E.; Sun, Y.; Aydin, F.; Zengin, H.; Turen, Y.; Ahlatci, H. Effects of Carbonaceous Reinforcements on Microstructure and Corrosion Properties of Magnesium Matrix Composites. *Mater. Chem. Phys.* **2018**, *218*, 182–188. [[CrossRef](#)]
11. Casati, R.; Vedani, M. Metal Matrix Composites Reinforced by Nano-Particles—A Review. *Metals* **2014**, *4*, 65–83. [[CrossRef](#)]
12. Lee, M.; Choi, Y.; Sugio, K.; Matsugi, K.; Sasaki, G. Effect of Aluminum Carbide on Thermal Conductivity of the Unidirectional CF/Al Composites Fabricated by Low Pressure Infiltration Process. *Compos. Sci. Technol.* **2014**, *97*, 1–5. [[CrossRef](#)]
13. Lim, J.Y.; Oh, S.I.; Kim, Y.C.; Jee, K.K.; Sung, Y.M.; Han, J.H. Effects of CNF Dispersion on Mechanical Properties of CNF Reinforced A7xxx Nanocomposites. *Mater. Sci. Eng. A* **2012**, *556*, 337–342. [[CrossRef](#)]
14. Diudea, M.V.; Szefer, B.; Nagy, C.L.; Bende, A. Exotic Allotropes of Carbon. In *Exotic Properties of Carbon Nanomatter: Advances in Physics and Chemistry*; Putz, M.V., Ori, O., Eds.; Springer: Dordrecht, The Netherlands, 2015; pp. 185–201.
15. Edie, D.D. The Effect of Processing on the Structure and Properties of Carbon Fibers. *Carbon* **1998**, *36*, 345–362. [[CrossRef](#)]
16. Xu, H.; Li, Q. Effect of Carbon Nanofiber Concentration on Mechanical Properties of Porous Magnesium Composites: Experimental and Theoretical Analysis. *Mater. Sci. Eng. A* **2017**, *706*, 249–255. [[CrossRef](#)]
17. Horzum, N.; Arik, N.; Truong, Y.B. Nanofibers for Fiber-Reinforced Composites. In *Fiber Technology for Fiber-Reinforced Composites*; Seydibeyoğlu, M.O., Mohanty, A.K., Misra, M., Eds.; Elsevier: Amsterdam, The Netherlands, 2017; pp. 251–275.
18. Abdo, H.S.; Khalil, K.A.; El-Rayes, M.M.; Marzouk, W.W.; Hashem, A.-F.M.; Abdel-Jaber, G.T. Ceramic Nanofibers versus Carbon Nanofibers as a Reinforcement for Magnesium Metal Matrix to Improve the Mechanical Properties. *J. King Saud Univ. Eng. Sci.* **2020**, *32*, 346–350. [[CrossRef](#)]
19. Seyedraoufi, Z.S.; Mirdamadi, S. Synthesis, Microstructure and Mechanical Properties of Porous Mg-Zn Scaffolds. *J. Mech. Behav. Biomed. Mater.* **2013**, *21*, 1–8. [[CrossRef](#)] [[PubMed](#)]
20. Burke, P.; Kipouros, G.J.; Fancelli, D.; Laverdiere, V. Sintering Fundamentals of Magnesium Powders. *Can. Metall. Quart.* **2009**, *48*, 123–132. [[CrossRef](#)]
21. De Mello, J.D.B.; Binder, R.; Klein, A.N.; Hutchings, I.M. Effect of Compaction Pressure and Powder Grade on the Microstructure, Hardness and Surface Topography of Steam Oxidized Sintered Iron. *Powder Metall.* **2006**, *44*, 248–254.
22. Mohammed, M.T.; Hussein, H.A.; Jasim, I.N.; Allawi, Z.I. Effect of Compaction Pressure on Morphology and Physical Properties for Cu-Based Produce by Using Powder Metallurgy Technique. Proceeding of the 1st International Scientific Conference of Engineering Sciences—3rd Scientific Conference of Engineering Science, ISCES, Diyala, Baqubah, Iraq, 10–11 January 2018; IEEE: New York, NY, USA, 2018; pp. 198–202.
23. Arifvianto, B.; Zhou, J. Fabrication of Metallic Biomedical Scaffolds with the Space Holder Method: A Review. *Materials* **2014**, *7*, 3588–3622. [[CrossRef](#)]
24. Goh, C.S.; Gupta, M.; Jarfors, A.E.W.; Tan, M.J.; Wei, J. Magnesium and Aluminium Carbon Nanotube Composites. *Key Eng. Mater.* **2010**, *425*, 245–261. [[CrossRef](#)]
25. Chui, P.; Jing, R.; Zhang, F.; Li, J.; Feng, T. Mechanical Properties and Corrosion Behavior of β -type Ti-Zr-Nb-Mo Alloys for Biomedical Application. *J. Alloys Compd.* **2020**, 155693. [[CrossRef](#)]
26. Yuangyai, C.; Nembhard, H.B. Design of Experiments: A Key to Innovation in Nanotechnology. In *Emerging Nanotechnologies for Manufacturing: A Volume in Micro and Nano Technologies*, 2nd ed.; Ahmed, W., Jackson, M.J., Eds.; Elsevier: Amsterdam, The Netherlands, 2010; pp. 207–234.
27. Gou, J.; Liang, Z.; Wang, B. Experimental Design and Optimization of Dispersion Process for Single-Walled Carbon Nanotube Bucky Paper. *Int. J. Nanosci.* **2004**, *3*, 293–307. [[CrossRef](#)]
28. Edrus, M.A.K.; Azman, M.S.M.; Tuminoh, H.; Nasution, A.K.; Ramlee, M.H. Fabrication and Characterization of Mg-Zn Alloys Reinforced with Carbon Nanofiber for Orthopaedics Implant Application: A Study on the Different Compositions. *Malays. J. Med. Health Sci.* **2020**, *83*, 1–6.
29. Tuminoh, H.; Azman, M.S.M.; Edrus, M.A.K.; Nasution, A.K.; Ramlee, M.H. Fabrication and Characterisation of Mg-Zn Alloys Reinforced with Cnf: A Study on the Sintering Process. *J. Teknol.* **2020**, *83*, 1–6. [[CrossRef](#)]
30. Salleh, E.M.; Ramakrishnan, S.; Hussain, Z. Synthesis of Biodegradable Mg-Zn Alloy by Mechanical Alloying: Effect of Milling Time. *Proc. Chem.* **2016**, *19*, 525–530. [[CrossRef](#)]
31. Vignesh, R.V.; Padmanaban, R.; Govindaraju, M. Study on the Corrosion and Wear Characteristics of Magnesium Alloy AZ91D in Simulated Body Fluids. *Bull. Mater. Sci.* **2020**, *43*, 8. [[CrossRef](#)]
32. Li, Q.; Rottmair, C.A.; Singer, R.F. CNT Reinforced Light Metal Composites Produced by Melt Stirring and by High Pressure Die Casting. *Compos. Sci. Technol.* **2010**, *70*, 2242–2247. [[CrossRef](#)]

33. Francis, R.; Kumar, D.S. *Biomedical Applications of Polymeric Materials and Composites*, 1st ed.; Wiley-VCH Verlag: Weinheim, Germany, 2016; pp. 125–140.
34. Wang, S.; Wei, X.; Xu, J.; Hong, J.; Song, X.; Yu, C.; Chen, J.; Chen, X.; Lu, H. Strengthening and Toughening Mechanisms in Refilled Friction Stir Spot Welding of AA2014 Aluminum Alloy Reinforced by Graphene Nanosheets. *Mater. Des.* **2020**, *186*, 108212. [[CrossRef](#)]
35. Meng, L.; Hu, X.; Wang, X.; Zhang, C.; Shi, H.; Xiang, Y.; Liu, N.; Wu, K. Graphene Nanoplatelets Reinforced Mg Matrix Composite with Enhanced Mechanical Properties by Structure Construction. *Mater. Sci. Eng. A* **2018**, *733*, 414–418. [[CrossRef](#)]
36. Liang, J.; Li, H.; Qi, L.; Tian, W.; Li, X.; Chao, X.; Wei, J. Fabrication and Mechanical Properties of CNTs/Mg Composites Prepared by Combining Friction Stir Processing and Ultrasonic Assisted Extrusion. *J. Alloys Compd.* **2017**, *728*, 282–288. [[CrossRef](#)]
37. Cai, S.; Lei, T.; Li, N.; Feng, F. Effects of Zn on Microstructure, Mechanical Properties and Corrosion Behavior of Mg–Zn Alloys. *Mater. Sci. Eng. C* **2012**, *32*, 2570–2577. [[CrossRef](#)]
38. Zou, N.; Li, Q. Effect of Compaction Pressure and Magnesium Weight Fraction on Hardness of Recycled-Polystyrene Matrix Composite. *JOM* **2018**, *70*, 1454–1458. [[CrossRef](#)]
39. Yusof, M.M.; Zuhailawati, H. The Effect of Compaction Pressure for on Properties of Binary and Ternary Magnesium Alloys. In *Proceeding of the 3rd International Conference of Global Network for Innovative Technology, Advance Materials for Innovative Technologies, Penang, Malaysia, 27–29 January 2016*; AIP: New York, NY, USA, 2017; p. 030005.
40. Rai, A.; Rai, P.; Kumar, V.; Singh, N.K.; Singh, V.K. Effect of Sintering Temperature on the Physico-Mechanical Behavior of SiC Reinforced Zinc-Magnesium Based Composite. *Met. Mater. Int.* **2020**, 1–9. [[CrossRef](#)]
41. Kumar, A.; Pandey, P.M. Development of Mg Based Biomaterial with Improved Mechanical and Degradation Properties Using Powder Metallurgy. *J. Magnes. Alloys* **2020**, *8*, 883–898. [[CrossRef](#)]
42. Wahi, A.; Muhamad, N.; Sulong, A.B.; Ahmad, R.N. Effect of Sintering Temperature on Density, Hardness and Strength of MIM Co30Cr6Mo Biomedical alloy. *Funtai Oyobi Fumatsu Yakini/J. Jpn. Soc. Powder Powder Metall.* **2016**, *63*, 434–437. [[CrossRef](#)]
43. Dlouhy, I.; Jang, G.J.; Yang, S.S.; Kim, Y.J.; Rudianto, H. Evaluation of Sintering Behavior of Premix Al-Zn-Mg-Cu Alloy Powder. *Adv. Mater. Sci. Eng.* **2015**, *2015*, 1–8.
44. Umasankar, V.; Anthony Xavier, M.; Karthikeyan, S. Experimental Evaluation of the Influence of Processing Parameters on the Mechanical Properties of SiC Particle Reinforced AA6061 Aluminium Alloy Matrix Composite by Powder Processing. *J. Alloys Compd.* **2014**, *582*, 380–386. [[CrossRef](#)]
45. Schaffer, G.; Hall, B.; Bonner, S.; Huo, S.; Sercombe, T. The Effect of the Atmosphere and the Role of Pore Filling on the Sintering of Aluminium. *Acta Mater.* **2006**, *54*, 131–138. [[CrossRef](#)]
46. Luo, X.; Fang, C.; Yao, F.; Zhao, H.; Yan, S. Effect of Sintering Parameters on the Microstructure and Mechanical Properties of Medical Mg–3Mn and Mg–3Zn Prepared by Powder Metallurgy. *Trans. Indian Inst. Metals* **2019**, *72*, 1791–1798. [[CrossRef](#)]
47. Mallireddy, N.; Siva, K. Investigation of Microstructural, Mechanical and Corrosion Properties of AA7010-TiB2 In-Situ Metal Matrix Composite. *Sci. Eng. Compos. Mater.* **2020**, *27*, 97–107. [[CrossRef](#)]
48. Samuel, R.; Kumar, P.S.; Robinson, S.D.S.; John, A.S. Corrosion Behaviour of Aluminium Metal Matrix Reinforced with Multi-Wall Carbon Nanotube. *J. Asian Ceram. Soc.* **2017**, *5*, 71–75. [[CrossRef](#)]
49. Ding, Y.F.; Lin, J.X.; Wen, C.E.; Zhang, D.M.; Li, Y.C. Mechanical Properties, Corrosion, and Biocompatibility of Mg-Zr-Sr-Dy Alloys for Biodegradable Implant Applications. *J. Biomed. Mater. Res. B* **2018**, *106*, 2425–2434. [[CrossRef](#)]
50. Tahmasebifar, A.; Kayhan, S.M.; Evis, Z.; Tezcaner, A.; Çinici, H.; Koç, M. Mechanical, Electrochemical and Biocompatibility Evaluation of AZ91D Magnesium Alloy as a Biomaterial. *J. Alloys Compd.* **2016**, *687*, 906–919. [[CrossRef](#)]
51. Niu, B.; Shi, P.; Wei, D.; Shanshan, E.; Li, Q.; Chen, Y. Effects of Sintering Temperature on the Corrosion Behavior of AZ31 Alloy with Ca–P Sol–Gel Coating. *J. Alloy. Compd.* **2016**, *665*, 435–442. [[CrossRef](#)]
52. Jafari, S.; Harandi, S.E.; Raman, R.S. A Review of Stress-Corrosion Cracking and Corrosion Fatigue of Magnesium Alloys for Biodegradable Implant Applications. *JOM* **2015**, *67*, 1143–1153. [[CrossRef](#)]
53. NACE; ASTM. G31—12a Standard Guide for Laboratory Immersion Corrosion Testing of Metals. *Phila. ASTM Int.* **2012**. [[CrossRef](#)]
54. Ramli, M.I.; Sulong, A.B.; Muhamad, N.; Muchtar, A.; Arifin, A.; Mohd Foudzi, F.; Al-Furjan, H.M.S. Effect of Sintering Parameters on Physical and Mechanical Properties of Powder Injection Moulded Stainless Steel-Hydroxyapatite Composite. *PLoS ONE* **2018**, *13*, e0206247. [[CrossRef](#)]